Journal of Analytical and Applied Pyrolysis 197 (2026) 107849

Contents lists available at ScienceDirect

Journal of Analytical and Applied Pyrolysis

journal homepage: www.elsevier.com/locate/jaap

Hydrogen-rich syngas production by pyrolysis-catalytic steam reforming of waste plastic over metal-loaded carbon catalysts

Yukun Li [a], Zhiheng Ma [b], Bingyang Li [b], Meiqian Chen [b,*], Hui Zhou [a,*], Paul T. Williams [c,*]

[a] Department of Energy and Power Engineering, Tsinghua University, Beijing 100084, China
[b] School of Mechanical, Electronic and Control Engineering, Beijing Jiaotong University, Beijing 100044, China
[c] School of Chemical & Process Engineering, University of Leeds, Leeds LS2 9JT, UK

ARTICLE INFO

Keywords:
Waste
Plastics
Pyrolysis: Catalysis
Reforming
Syngas

ABSTRACT

The pyrolysis-catalytic steam reforming of waste plastic offers a promising route for the sustainable production of hydrogen-rich syngas. In this study, a series of carbon-supported metal catalysts (Zn/C, Cu/C, and Fe/C) with a nominal metal loading of 5 wt% were prepared and systematically evaluated for the pyrolysis-catalytic steam reforming of high-density polyethylene in a two-stage reactor system. The structural evolution of fresh and used catalysts was comprehensively characterized using scanning electron microscopy coupled with energy-dispersive X-ray spectroscopy, X-ray diffraction, and N_2 physisorption analyses. The carbon support provides a porous and thermally stable framework that enables uniform metal dispersion and minimizes structural interference, allowing the catalytic roles of different metal species to be systematically evaluated. The results demonstrate that metal species distinctly regulate product distribution, carbon conversion pathways, and hydrogen potential, following the order of Fe/C > Cu/C > Zn/C. Density functional theory (DFT) calculations reveal that these differences originate from the coupled effects of hydrocarbon activation and water dissociation on metal surfaces. This work establishes a clear structure-performance-mechanism relationship and provides mechanistic insights for the rational utilization of metal-containing waste-derived char catalysts in pyrolysis-catalytic steam reforming systems.

1. Introduction

With the continuous growth of global plastic production, the large-scale accumulation of plastic waste has become an increasingly urgent environmental challenge. It is estimated that by 2050, approximately 12 billion tonnes of plastic will accumulate in landfills or be released into the natural environment worldwide, posing long-term risks to ecosystems and human health [1]. High-density polyethylene (HDPE), one of the most widely produced and used polyolefin plastics, is difficult to manage sustainably through traditional mechanical recycling or landfill disposal due to its stable chemical structure and poor environmental degradability [2]. To address the challenges posed by the large volume of plastic waste and its limited recyclability, research efforts have increasingly focused on the high-value utilization of plastic waste through thermochemical conversion technologies. Many studies [3–7] have demonstrated that waste plastics can be transformed into a range of value-added products, including hydrocarbon fuels, hydrogen-rich syngas and high-value carbon materials. Such approaches offer a promising route to mitigating plastic pollution while simultaneously enabling energy recovery and material recycling.

Over the past two decades, research on the thermochemical conversion of plastic waste has gradually shifted from producing synthetic oils and liquid fuels to efficiently generating hydrogen. This change in research focus is largely attributed to the inherent advantages of plastic as a hydrogen-rich feedstock, with hydrogen contents typically in the range of 8–14 wt%, providing a favorable material basis for the production of hydrogen-rich gases [2]. On this basis, several research groups [8–12] have proposed and systematically developed two-stage pyrolysis-catalytic steam reforming processes for the production of hydrogen-rich syngas from waste plastics. In such processes, the plastic is typically pyrolyzed in the range of 550–600 °C to generate volatile hydrocarbons, which are subsequently converted into syngas (H_2+CO) via catalytic steam reforming at 800 °C [8–12]. The integrated approach effectively couples waste plastic management with clean energy

* Corresponding authors.
E-mail addresses: mqchen@bjtu.edu.cn (M. Chen), huizhou@tsinghua.edu.cn (H. Zhou), p.t.williams@leeds.ac.uk (P.T. Williams).

https://doi.org/10.1016/j.jaap.2026.107849
Received 17 February 2026; Received in revised form 14 April 2026; Accepted 6 May 2026
Available online 8 May 2026

production, harnessing the conversion of high-molecular-weight polymer waste into small-molecule, clean gaseous fuels.

In the pyrolysis-catalytic steam reforming process, the catalyst plays a crucial role in converting pyrolysis volatiles, regulating reaction pathways, and optimizing product distribution. An appropriate catalyst can not only significantly promote the cracking and reforming of large-molecule hydrocarbons and tar, thereby enhancing hydrogen yield and selectivity, but also play an important role in inhibiting carbon deposit formation and delaying catalyst deactivation [13]. To date, catalysts used in the steam reforming process have commonly included metal oxide-, zeolite-, and porous carbon-based catalysts.

Metal oxide-based catalysts, particularly Al_2O_3-supported transition metals such as Ni, Fe, and Co, have been widely applied in hydrocarbon reforming due to their excellent thermal stability, strong C-C bond cleavage and favorable water-gas shift activity [14–17]. The introduction of promoter metals, such as Ce and La, has been shown to improve metal dispersion further, enhance resistance to carbon deposition, and improve overall catalytic stability [18]. In addition, zeolite-based catalysts, with well-defined pore structures and strong acidity, exhibit excellent performance in hydrocarbon cracking reactions and in regulating product distribution [19].

However, the synthesis of metal-based and zeolite-based catalysts is often associated with relatively high preparation costs and limited resistance to deactivation under reforming conditions. In contrast, porous carbon-based materials have gained attention in recent years due to their wide availability, low cost, and good thermal stability. Previous studies [20–22] have found that waste-derived char (such as tire char, biochar, and refuse-derived fuel char) contains natural metal components such as Zn, Fe, Ca, Cu, Al, etc., and can significantly enhance hydrogen production in the steam reforming of plastic pyrolysis volatiles. For example, when using tire char as a catalyst in catalytic steam reforming of HDPE pyrolysis volatiles at 900 °C, the hydrogen yield reaches 73 mmol g^{-1} [20]. The catalytic performance of the char materials is usually attributed to their developed pore structure and the presence of intrinsic metal species. However, due to the diverse types and complex compositions of metal elements in waste-derived chars, it remains challenging to clearly identify the independent catalytic roles of individual metal elements. Consequently, the specific contributions of different metal species to the steam reforming reaction, the regulation of syngas components, and the carbon conversion process are still not clearly understood.

In recent years, DFT has become an important theoretical tool for revealing catalytic mechanisms, as it enables the exploration of bond-breaking processes and energy changes in chemical reactions at the molecular level [23,24]. For metal-supported catalytic systems, differences in electronic structure induced by different metals on the support surface can significantly influence reactant adsorption energies and transition-state energy barriers, thereby determining the reaction pathway and rate. Consequently, DFT has been widely applied to comprehensively seek the regulatory role of metal surfaces on the decomposition behavior of hydrocarbons. For instance, Chen et al. [25] used DFT to study the interactions and decomposition mechanisms of three common tar model compounds on a Ni (111) surface, and they pointed out that benzene undergoes initial dehydrogenation as the primary decomposition step, while toluene and phenol tend to experience substituent dehydrogenation before the aromatic ring breakage. Wei et al. [26] used DFT to address the catalytic cracking mechanism of biomass model compounds during steam reforming over Ni- and Fe-doped CaO surface, revealing distinct roles of the two metals in stabilizing hydrogen radicals and promoting surface reactions. By enhancing chemical adsorption strength, modifying the electronic structure, inducing low-energy-level migration, and generating new electronic states, Ni- and Fe-doped CaO surfaces provide a favorable electron environment for tar catalytic cracking, effectively lowering the reaction energy barrier and improving reaction efficiency and selectivity. Therefore, combining the experimental approach with DFT calculations offers a deeper understanding of the properties of intermediate products and transition states, reaction energies, and the identification of favorable reaction pathways for generating the target products [26–28].

In this study, a metal-free carbon material was selected as an inert and structurally stable support, onto which Zn, Fe, and Cu were individually loaded to construct a series of carbon-based catalysts. By using a uniform carbon support and only modifying the metal species, this study effectively decoupled the support structure effect from the intrinsic catalytic properties of the metals, enabling direct comparisons and in-depth analysis of the catalytic effects of different metals. Particular attention was paid to how different metals regulate syngas formation, carbon conversion pathways, and the activation of key hydrocarbon intermediates. In addition, the relationship between catalyst structure, catalytic performance, and reaction mechanism was investigated to provide mechanistic insight into the catalytic behavior of metal-containing waste-derived chars and to support the rational design of carbon-based catalysts for hydrogen-rich syngas production from waste plastics. The research was carried out using a two-stage pyrolysis-catalytic steam reforming reactor to produce syngas from waste plastic (high-density polyethylene). This two-stage configuration is particularly suitable for plastics, as they first melt and thermally decompose into volatile hydrocarbons, which can then be more effectively converted into syngas in a downstream catalytic reforming stage. In addition, the two-stage process enables more specific and independent control of the pyrolysis process and the catalytic steam reforming process.

2. Materials and methods

2.1. Materials and catalyst

High-density polyethylene pellets with an average particle size of approximately 2 mm were supplied by Regain Polymers Limited (Castleford, UK) and used as the feedstock in this study. The HDPE used in this study was a recycled plastic material, recovered from 'real-world' waste plastics. A high-purity carbon material was purchased from Sigma-Aldrich and used as the catalyst support. The total content of metal impurities (Al, Ti, Fe, Ni, Cu, and Zn) in the carbon support was below 100 ppm, indicating it was nearly metal-free and inert.

Metal-loaded catalysts were prepared by wet impregnation. Specifically, appropriate amounts of $Zn(NO_3)_2{\cdot}6\ H_2O$, $Fe(NO_3)_3{\cdot}9\ H_2O$, and $Cu(NO_3)_2{\cdot}2.5\ H_2O$ were dissolved in deionized water to form the corresponding precursor solutions. The carbon support was then added to each solution and continuously stirred at 80 °C until a homogeneous slurry was obtained. The slurry was dried at 105 °C for 12 h to remove moisture, followed by calcination at 800 °C for 3 h under a nitrogen atmosphere. The nominal metal loading was intentionally fixed at 5 wt% to ensure sufficient surface metal sites for mechanistic comparison, rather than to maximize catalytic activity. The resulting catalysts were denoted as Zn/C, Fe/C, and Cu/C, respectively. The carbon support without metal loading was used as a reference catalyst and denoted as Carbon. It should be noted that the catalyst was designed using the same high-purity carbon support and the same nominal metal loading, so that the observed differences could be mainly associated with metal identity rather than compositional variations of the support.

2.2. Catalyst characterization

The surface morphology of the catalysts was characterized using a scanning electron microscope (SEM, JSM-7900F, JEOL), and the elemental distribution was analyzed by energy-dispersive X-ray spectroscopy (EDX, Oxford Instruments). The crystalline phases and structural properties were determined by X-ray diffraction (XRD, Empyrean, PANalytical) using Cu Kα radiation. The specific surface area and pore structure parameters were obtained from N_2 adsorption-desorption measurements using a Micromeritics TriStar 3000 instrument. The

specific surface area was calculated according to the Brunauer-Emmett-Teller (BET) method, while the pore size distribution and pore volume were derived from the Barrett-Joyner-Halenda (BJH) model.

2.3. Experimental reactor and procedure

A two-stage fixed-bed reactor system comprising a pyrolysis reactor and a downstream catalytic reactor was used in this study (Fig. 1). High-purity nitrogen was used as the inert carrier gas, with a flow rate of 100 mL min^{-1}. For each experiment, 1.0 g of HDPE was weighed and suspended in the pyrolysis reactor, while 1.0 g of catalyst was placed in the catalytic reactor. Once the catalytic reactor reached 800 °C and stabilized, the pyrolysis reactor was heated to 600 °C at a heating rate of 20 °C min^{-1} and maintained at this temperature for 20 mins.

During this process, HDPE underwent thermal decomposition, generating volatiles that were transported by the carrier gas into the catalytic reactor. In the catalytic stage, water was continuously injected using a syringe pump to generate steam at a flow rate of 8 mL h^{-1}. The pyrolysis volatiles were subsequently reformed with steam over the catalyst to produce gaseous products. The produced gases passed through a three-stage condensation system to remove condensable components, and the resulting gas was finally collected in gas sampling bags for offline analysis by gas chromatography.

2.4. Product analysis

The gaseous products were identified and quantified by gas chromatography (GC). Light hydrocarbons (C_1-C_4) were detected using a Varian CP-3380 GC equipped with a flame ionization detector (FID), while permanent gases (H_2, CO, N_2, and CO_2) were analyzed using another GC equipped with a thermal conductivity detector (TCD). To ensure the reliability of the experimental results, each experiment was repeated three times, and the reported values represent the average of the measurements.

The gas yield was defined as the ratio of the total mass of gaseous products generated after the reaction to the total mass of the inputs in the pyrolysis-catalytic steam reforming system, as calculated using Eq.1. The liquid yield was defined as the mass fraction of condensed water together with a small amount of unconverted tar relative to the total input mass, while the solid yield corresponded to the mass fraction of pyrolysis residues and carbonaceous deposits formed on the catalyst, as calculated using Eqs.2 and 3. The overall mass balance was calculated according to Eq.4 from the sum of gas, liquid and solid yield. For all experiments, the mass balance closure was close to 100 wt%, with deviations below 2%. The carbon conversion was defined as the fraction of carbon in the feedstock converted into gaseous products and was calculated using Eq.5. The H_2 potential was defined as the ratio of the experimentally obtained hydrogen yield to the theoretical maximum hydrogen yield assuming all of the carbon and hydrogen in HDPE is converted to H_2 and CO_2 via the steam reforming process [8] and was calculated using Eq.6. It should be noted that the reported product yields and gas compositions represent cumulative results collected over the full experimental run, rather than instantaneous values at zero time on stream.

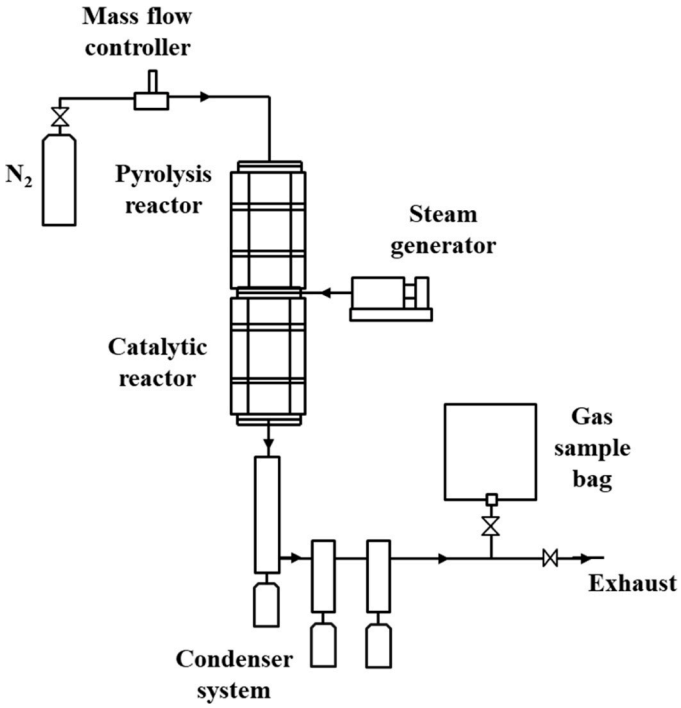

Fig. 1. Schematic diagram of the pyrolysis-catalytic steam reforming reactor.

$$Gas\ yield_{total}\ (wt.\%) = \frac{\sum m_{each\ gas}}{m_{plastic} + m_{water}} \quad (1)$$

$$Liquid\ yield_{total}\ \ (wt.\%) = \frac{\sum m_{liquid}}{m_{plastic} + m_{water}} \quad (2)$$

$$Solid\ yield_{total}\ \ (wt.\%) = \frac{\sum m_{residue}}{m_{plastic} + m_{water}} \quad (3)$$

$$Mass\ balance = Gas\ yield_{total} + Liquid\ yield_{total} + Solid\ yield_{total} \quad (4)$$

$$C_{conversion} = \frac{mass\ of\ C\ in\ each\ gas}{mass\ of\ C\ in\ feedstcok} \quad (5)$$

$$H_2\ potential\ \ (\%) = \frac{Experimental\ H_2\ yield}{Theoretical\ H_2\ yield} \quad (6)$$

2.5. DFT calculation

All spin-polarized density functional theory calculations in this work were carried out with the Vienna Ab-initio Simulation Package (VASP) [29]. The electron-ion interactions were described by the projector augmented wave (PAW) method, and the exchange-correlation functional was treated within the generalized gradient approximation (GGA) by the Perdew-Burke-Ernzerhof (PBE) formulation [30]. Grimme's DFT-D3 semi-empirical dispersion correction was included to properly account for weak interactions (e.g., van der Waals forces) between adsorbates and metal surfaces [31]. Periodic slab models were constructed to investigate the energy barriers for the dehydrogenation of ethylene molecules and water molecules, as well as the reactions between ethylene and OH* species on Fe, Cu, and Zn surfaces. A vacuum layer of at least 15 Å was applied perpendicular to the surface to avoid spurious interactions between periodic images. The Brillouin zone was sampled using the Monkhorst-Pack scheme with a $6 \times 6 \times 1$ k-point mesh. A plane-wave kinetic energy cutoff of 520 eV was used. The electronic self-consistent field calculations were considered converged when the energy change was below 1×10^{-5} eV, and the geometry optimizations were terminated when the residual force on each atom was less than 0.05 eV $Å^{-1}$.

The geometry of all reactants, products, and intermediates was fully optimized. Transition states (TSs) of the elementary reactions were located via the climbing image nudged elastic band (CI-NEB) method, and their validity was confirmed by vibrational frequency analysis [32]. Each TS exhibited exactly one imaginary frequency, and the corresponding vibrational mode was visually inspected to ensure that it matched the expected bond-breaking or bond-forming process along the reaction coordinate. The activation energy (E_a) was defined as the total energy difference between the TS and the corresponding reactant state. The methodology provides reliable kinetic barrier information to

elucidate the intrinsic mechanisms of surface-catalyzed reactions. All calculations were conducted under well-converged conditions to ensure the accuracy and reproducibility of the results.

3. Results and discussion

3.1. Characterization of fresh catalysts

Fig. 2 presents the SEM images of the fresh catalysts and the corresponding EDX spectrometry elemental mapping results. As shown in

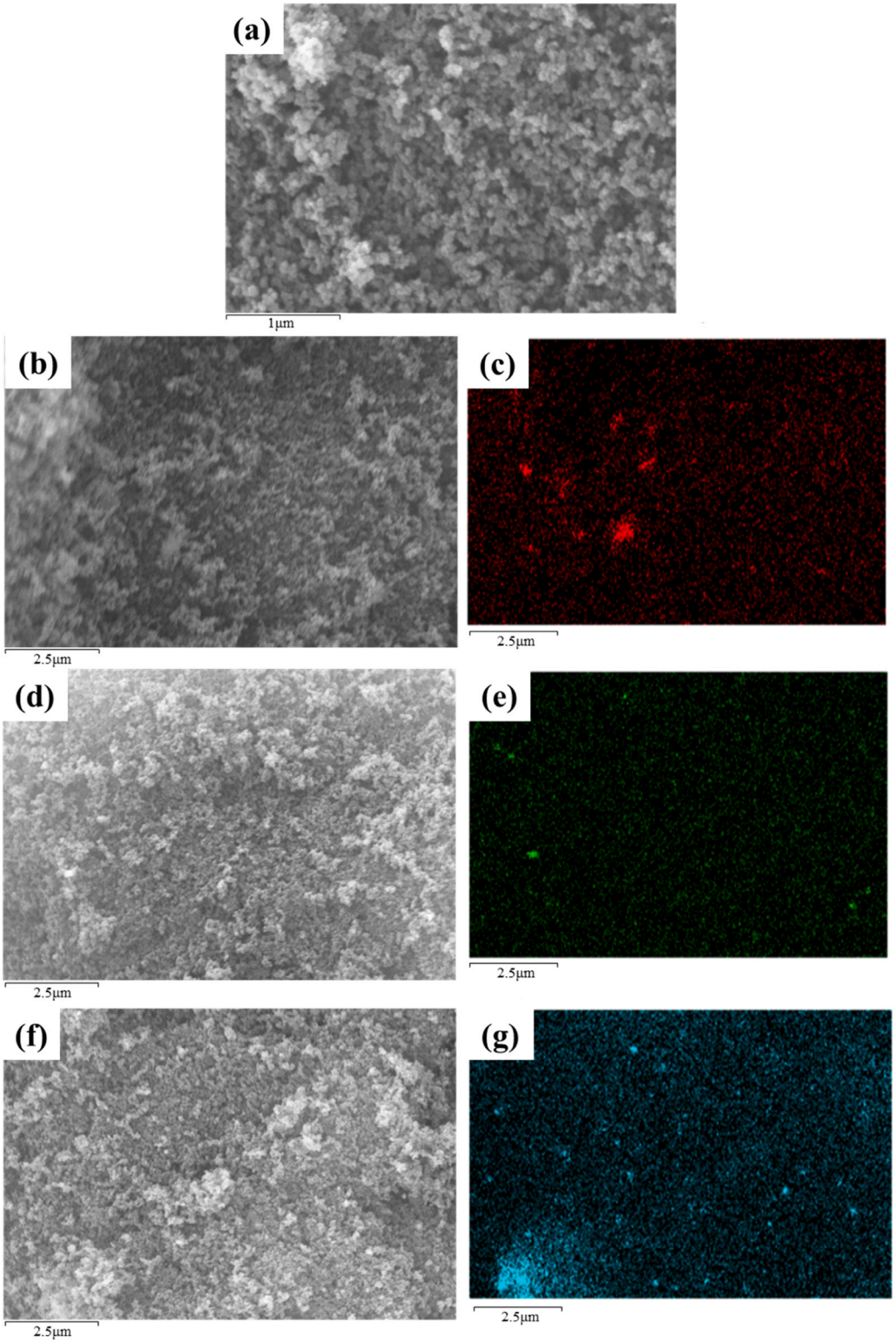

Fig. 2. SEM images and corresponding EDX elemental mapping of the fresh catalysts. (a) SEM image of the metal-free fresh carbon; (b) SEM image of fresh Zn/C; (c) EDX elemental mapping of Zn; (d) SEM image of fresh Fe/C; (e) EDX elemental mapping of Fe; (f) SEM image of fresh Cu/C; and (g) EDX elemental mapping of Cu.

Fig. 2(a), the fresh carbon support exhibits an irregular rough surface morphology, composed of aggregated carbon particles. The textural properties of the support are discussed in more detail based on BET analysis. Such a rough and heterogeneous surface is favorable for metal deposition, while the textural characteristics relevant to volatile adsorption and diffusion are more appropriately reflected by the BET surface area and pore volume data. This porous texture is favorable for the adsorption and diffusion of pyrolysis volatiles and provides abundant anchoring sites for subsequent metal loading. No obvious metallic signals were detected for the fresh carbon support in the SEM-EDX analysis, consistent with the high purity of the commercial carbon support described in 2.1.

After metal impregnation, all catalysts retain a similar porous carbon framework, indicating that the impregnation and calcination processes do not induce noticeable structural damage or morphological collapse of the support. The Zn/C catalyst (Fig. 2(b)) maintains a porous surface without the presence of large crystalline particles or severe agglomeration, while the corresponding Zn elemental mapping (Fig. 2(c)) shows a relatively uniform spatial distribution of Zn species over the carbon surface. Likewise, the Fe/C catalyst (Fig. 2(d)) preserves the original porous morphology of the carbon support and the Fe elemental mapping (Fig. 2(e)) reveals a homogeneous dispersion of Fe species without the formation of obvious micron-scale aggregates, suggesting a high degree of metal dispersion that is favorable for generating accessible active sites. In contrast, although the Cu/C catalyst (Fig. 2(f)) exhibits a surface morphology comparable to those of Zn/C and Fe/C, the Cu elemental mapping (Fig. 2(g)) shows intensified signals locally, suggesting partial local enrichment or slight agglomeration of Cu species. This localized aggregation may affect the distribution and accessibility of active sites, thereby influencing catalytic performance.

Overall, the SEM-EDX results confirm that Zn, Fe, and Cu were successfully loaded onto the carbon support without causing structural collapse or morphological damage. The comparable surface morphologies among the different metal-loaded catalysts provide a consistent structural basis for evaluating catalytic performance, enabling the observed differences in reaction performance to be attributed mainly to the properties of the metal species rather than to changes in the support morphology.

Fig. 3 shows the XRD patterns of the fresh carbon support and the metal-loaded catalysts. The fresh carbon exhibits a broad and weak diffraction peak centered at 2θ≈ 20–25°, which is characteristic of the (002) reflection of amorphous or poorly graphitized carbon, consistent with previous reports on porous carbon materials [33,34]. This low degree of structural ordering is typically associated with abundant surface defects, which can facilitate the anchoring and dispersion of metal species and promote the adsorption of volatiles. For the Zn/C catalyst, several weak and broadened diffraction peaks are observed and can be indexed to the wurtzite structure of ZnO [35]. The low intensities and broad peak shapes indicate that Zn species are mainly present as highly dispersed nanocrystalline oxides rather than forming large crystalline grains. In the case of Fe/C catalyst, weak diffraction peaks in the range of 2θ≈ 35–45° are detected, corresponding to poor crystalline iron oxide phases, which have been commonly reported for carbon-supported Fe catalysts [36]. The broad peaks indicate that Fe species remain highly dispersed and may interact strongly with the carbon support. These metal-support interactions are generally considered favorable for stabilizing active species and inhibiting sintering at high temperatures [37,38]. The observed oxidation states of Zn and Fe are mainly determined by their intrinsic thermodynamic stability and by strong metal-support interactions during high-temperature treatment. Compared with Zn/C and Fe/C, the Cu/C catalyst shows sharper and more intense diffraction peaks at 2θ ≈ 43.3°, 50.4° and 74.1°, which can be assigned to metallic Cu according to standard PDF references. The higher peak intensity and sharpness indicate higher crystallinity and a relatively larger crystallite size of the Cu species, consistent with the local enrichment observed in SEM-EDX analysis.

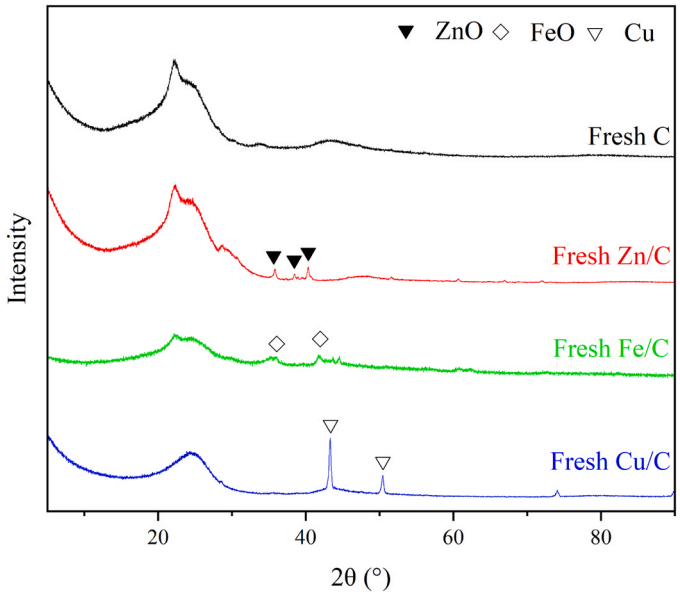

Fig. 3. XRD patterns of the fresh catalysts.

Table 1 summarizes the BET (Brunauer-Emmett-Teller) surface area and pore volume of the fresh carbon support and the metal-loaded catalysts. The pure carbon exhibits a specific surface area of 217.6 m^2 g^{-1} and a total pore volume of 0.44 cm^3 g^{-1}, indicating a well-developed porous structure, consistent with the SEM observations. After metal loading, the specific surface areas of Zn/C, Fe/C and Cu/C slightly increase to 237.8, 233.5, and 233.9 m^2 g^{-1}, respectively, while the corresponding pore volumes remain nearly unchanged (0.44–0.46 cm^3 g^{-1}). The absence of significant surface area loss or pore volume reduction after metal loading indicates that metal impregnation does not cause pore blockage or structural collapse. The slight increase in surface area may be attributed to the release of gaseous species during nitrate decomposition and the generation of additional surface defects during thermal treatment. More importantly, the three metal-loaded catalysts exhibit highly comparable surface areas and pore volumes, ensuring a consistent textural background for catalytic performance evaluation. Consequently, the differences in catalytic activity and product distribution observed in subsequent sections can be primarily attributed to the intrinsic chemical properties of the metal species and their interactions with reaction intermediates, rather than differences in the pore structure of the carbon support.

3.2. *Influence of metal species on product yields and gas composition*

Table 2 summarizes the overall product distribution and water reaction amount during the pyrolysis-catalytic steam reforming of HDPE at a temperature of 800 °C in relation to different catalyst systems. All product yields were calculated based on the total mass input of the system. It should be noted that the liquid products mainly consist of unreacted water and a trace amount of incompletely reformed tar, indicating a high overall conversion efficiency and a mass balance close to 100%. As shown in Table 2, the introduction of metal species has a

Table 1
Physical properties of the freshly prepared catalysts.

	BET surface area (m^2/g)	Pore volume (cm^3/g)
Fresh Carbon	217.6	0.44
Fresh Zn/C	237.8	0.45
Fresh Fe/C	233.5	0.46
Fresh Cu/C	233.9	0.44

Table 2
Product distribution from pyrolysis-catalytic steam reforming of HDPE at 800 °C in the presence of carbon catalysts with different metals.

	Carbon	Zn/Carbon	Cu/Carbon	Fe/Carbon
Gas yield (wt%)	20.70	20.75	21.07	21.61
Liquid yield (wt%)	80.99	78.93	76.25	75.12
Reacted water (g)	0.56	0.72	0.90	1.05

significant impact on the gas yield. Compared with the pure carbon catalyst, the gas yields from processing of plastic in the Cu/C and Fe/C systems increase to 21.07 wt% and 21.61 wt% respectively, indicating that these two metals are more effective in promoting the secondary conversion of pyrolysis volatiles and steam reforming reactions. This enhancement is commonly attributed to the strong adsorption capability of transition metals towards hydrocarbon intermediates and their ability to facilitate C-H and C-C bond breakage [39,40]. In addition to gas yield, water consumption can serve as a key indicator of the activity of steam reforming reactions. As listed in Table 2, the amount of water consumed increases markedly upon metal loading and follows the order of Fe/C > Cu/C > Zn/C > Carbon. Among all catalysts, the water consumption in the Fe/C system is the highest (1.05 g), indicating that the Fe species has a stronger ability to activate water molecules and promote water participation in surface reactions. Previous research [41] has reported that Fe-based catalysts can effectively dissociate water to generate surface hydroxyl and active hydrogen species, which further participate in hydrocarbon reforming and water-gas shift reaction.

Fig. 4(a) compares the gas yield from pyrolysis-catalytic steam reforming of HDPE under different metal-loaded carbon catalysts. It is evident that the introduction of metal-loaded catalysts significantly enhances H_2 and CO yields, in the order Fe/C > Cu/C > Zn/C > Carbon. In particular, the H_2 yield was highest in the Fe/C system and lowest in the pure carbon system, indicating that the metal species played a key role in promoting the cracking, dehydrogenation, and secondary reforming reactions of hydrocarbon intermediates. This difference can be attributed to the different adsorption and activation abilities of different metals on the reaction intermediates. Transition metals such as Fe and Cu possess partially filled d orbitals that can strongly interact with the π and σ bonds of hydrocarbon molecules, thereby reducing the energy barrier to breaking C-C and C-H bonds and promoting deep cracking and reforming reactions [26]. In contrast, Zn species exhibit a relatively weaker interaction with hydrocarbons, resulting in a limited promotional effect.

The gas composition from the pyrolysis-catalytic steam reforming of HDPE shown in Fig. 4(b) further reveals that metal loading not only increases the total gas yield but also substantially alters the reaction pathway. With the introduction of metals, the volumetric fraction of H_2 in the gas mixture significantly increases, while the fractions of CO_2 and CH_4 decrease correspondingly, indicating a shift towards hydrogen-rich syngas production. Among the catalysts investigated, the Fe/C system exhibits the highest H_2 concentration, suggesting a stronger ability to undergo deep dehydrogenation and steam-assisted reactions. This behavior is consistent with the high-water activation ability and strong redox performance of Fe-based catalysts in steam reforming systems [42].

To further evaluate the practical application potential of the produced gas, Fig. 4(c) presents the yield of syngas (H_2+CO) for each system. The Fe/C catalyst exhibits the highest syngas yield, followed by Cu/

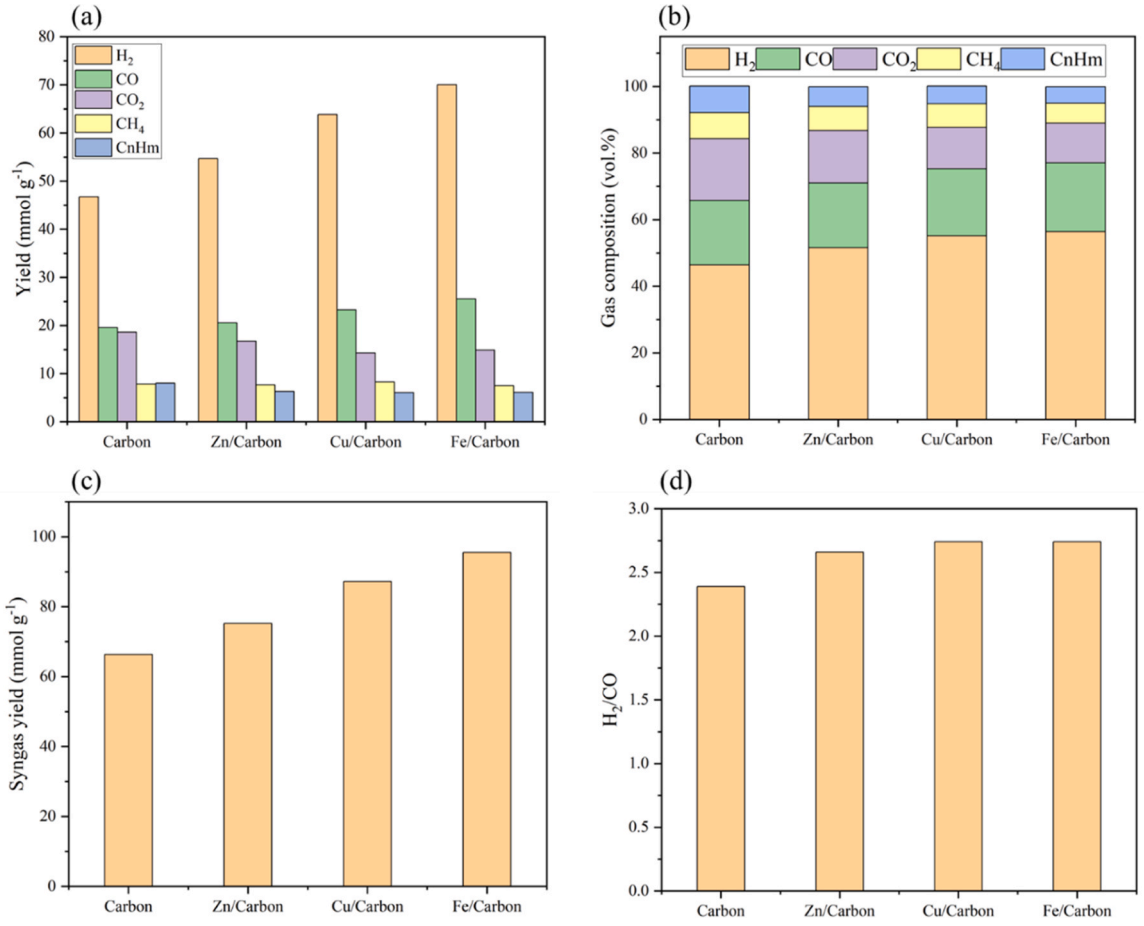

Fig. 4. Effect of different metal-loaded carbon catalysts on (a) gas yield, (b) gas composition, (c) syngas yield and (d) H_2/CO ratio during pyrolysis-catalytic steam reforming of HDPE.

C and Zn/C, while the pure carbon system shows the lowest performance. This trend is consistent with the aforementioned changes in individual gas yields, confirming that metals incorporation significantly improves the conversion efficiency of carbon toward syngas. Additionally, the composition of the syngas is a critical parameter for downstream utilization. As shown in Fig. 4(d), all metal-loaded catalysts significantly increase the H_2/CO ratio compared with the pure carbon system, with Fe/C and Cu/C systems showing higher values of approximately 2.74. This higher H_2/CO ratio is more suitable for downstream processes such as Fischer-Tropsch synthesis and methanol production [43]. Notably, the H_2/CO ratio is not only governed by hydrocarbon cracking and reforming reactions but is also strongly influenced by the water-gas shift reaction. Combining the trend in water consumption in Table 2, the higher H_2/CO ratio observed over the Fe/C system can be reasonably attributed to its enhanced water-activation capability, which promotes water dissociation and subsequent hydrogen generation.

3.3. Carbon conversion and hydrogen potential

Fig. 5(a) illustrates the distribution of carbon converted into different gaseous products (CO, CO_2, CH_4, and C_2-C_4) during the pyrolysis-catalytic steam reforming of HDPE over different catalysts. When pure carbon is used as the catalyst, the conversion of carbon to CO is the lowest, while the conversion to CO_2 is the highest, indicating that the reaction system preferentially follows incomplete reforming or deep oxidation pathways. With the introduction of metals, a pronounced shift in the carbon conversion pathway is observed. The conversion of carbon to CO significantly increases, accompanied by a corresponding decrease in carbon conversion to CO_2. This trend indicates that metal incorporation alters the reaction network, making the system more inclined to generate CO through steam reforming and partial oxidation pathways rather than complete oxidation to CO_2. It should be noted that this phenomenon does not suggest a direct catalytic conversion of CO_2 to CO by the metals, but rather results from an overall shift in the reaction pathway distribution, with more carbon intermediates being converted to CO via steam reforming pathways, thereby indirectly suppressing the formation of CO_2. Simultaneously, the conversion of carbon to light hydrocarbons such as C_2-C_4 decreases markedly upon metal loading, indicating that metals effectively promoted the secondary reforming of light hydrocarbons. This trend is consistent with the higher H_2 and CO yields observed in the metal-loaded catalysts in 3.2. In contrast, the conversion of carbon to CH_4 shows no significant change among different catalysts, indicating that methane is not the primary controlled species in this system. Instead, the catalytic role of metals is mainly associated with the activation and reforming of higher-carbon-number hydrocarbons (C_2+), as reported in various steam reforming systems, where transition metals exhibit greater activation of C_2+ hydrocarbons than methane [44].

Fig. 5(b) presents the hydrogen potential under different catalytic conditions. The introduction of metals leads to a substantial increase in hydrogen potential, following the order Fe/C > Cu/C > Zn/C > Carbon. This trend indicates that metals not only enhance the absolute hydrogen yield (see 3.2) but also improve the hydrogen generation efficiency per unit of carbon converted. This phenomenon can be attributed to two synergistic effects: (i) metals promote the deep dehydrogenation and reforming of hydrocarbon intermediates; and (ii) metals facilitate the activation of water molecules, enabling more hydrogen atoms to be converted to molecular hydrogen through steam reforming and water-gas shift reactions. Among them, the Fe/C system exhibits the highest hydrogen potential, which is highly consistent with the highest water consumption trend shown in Table 2, further confirming the advantage of Fe species in water molecule dissociation and active hydrogen generation. The above results indicate that different metals regulate both the mode of carbon conversion and hydrogen generation efficiency by changing reaction pathways and controlling the extent of water participation in the reforming process.

3.4. Evolution of catalyst structure and surface properties after reaction

Fig. 6 presents the SEM morphologies and corresponding EDX elemental distribution. Generally speaking, compared with fresh catalysts, used catalysts retain a porous structure characterized by aggregated carbon particles, with no apparent pore collapse or formation of a dense surface layer. This indicates that the carbon support exhibits good structural stability under high-temperature steam reforming conditions. Therefore, the differences in catalytic performance observed in this system cannot be attributed to drastic changes in macroscopic morphology, but are more likely related to the chemical state and evolution behavior of the metal species during the reaction.

For the used carbon catalysts, the surface morphology after the reaction remains unchanged compared with the fresh catalyst, still exhibiting a rough, porous structure formed by irregular particle aggregation. The corresponding elemental analysis confirms the absence of metallic elements, indicating that no exogenous metal migration occurs during the reaction. This sample thus provides a reliable structural reference for comparison with metal-loaded catalysts. In the case of used Zn/C (Fig. 6(b)-(c)), Zn species are still distributed over the entire observation area, but a few local high-intensity bright spots can be observed, indicating that Zn species have a local enrichment or redistribution after the reaction. Combined with the absence of large

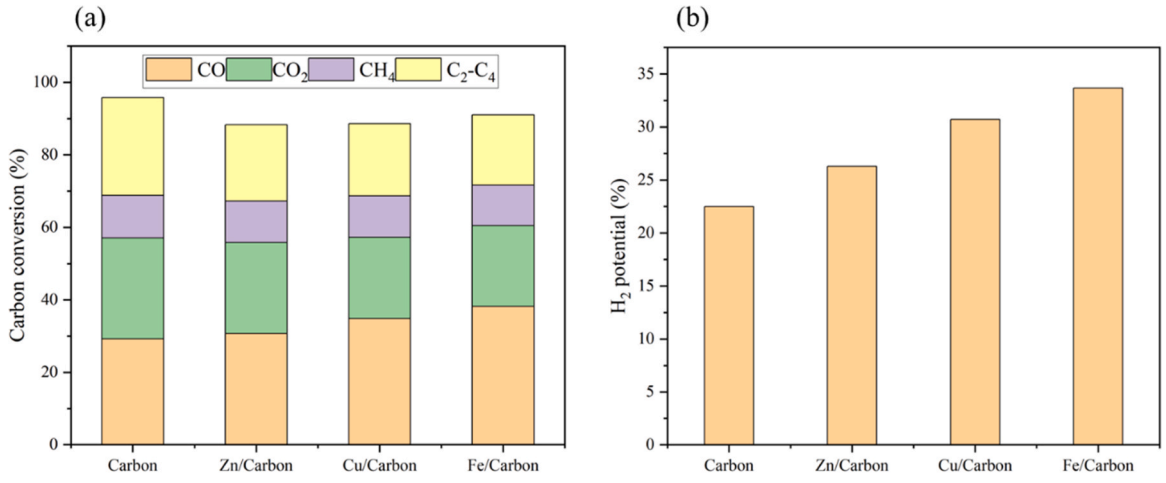

Fig. 5. Effect of metal-loaded carbon catalysts on carbon conversion pathways and H_2 potential during pyrolysis-catalytic steam reforming of HDPE.

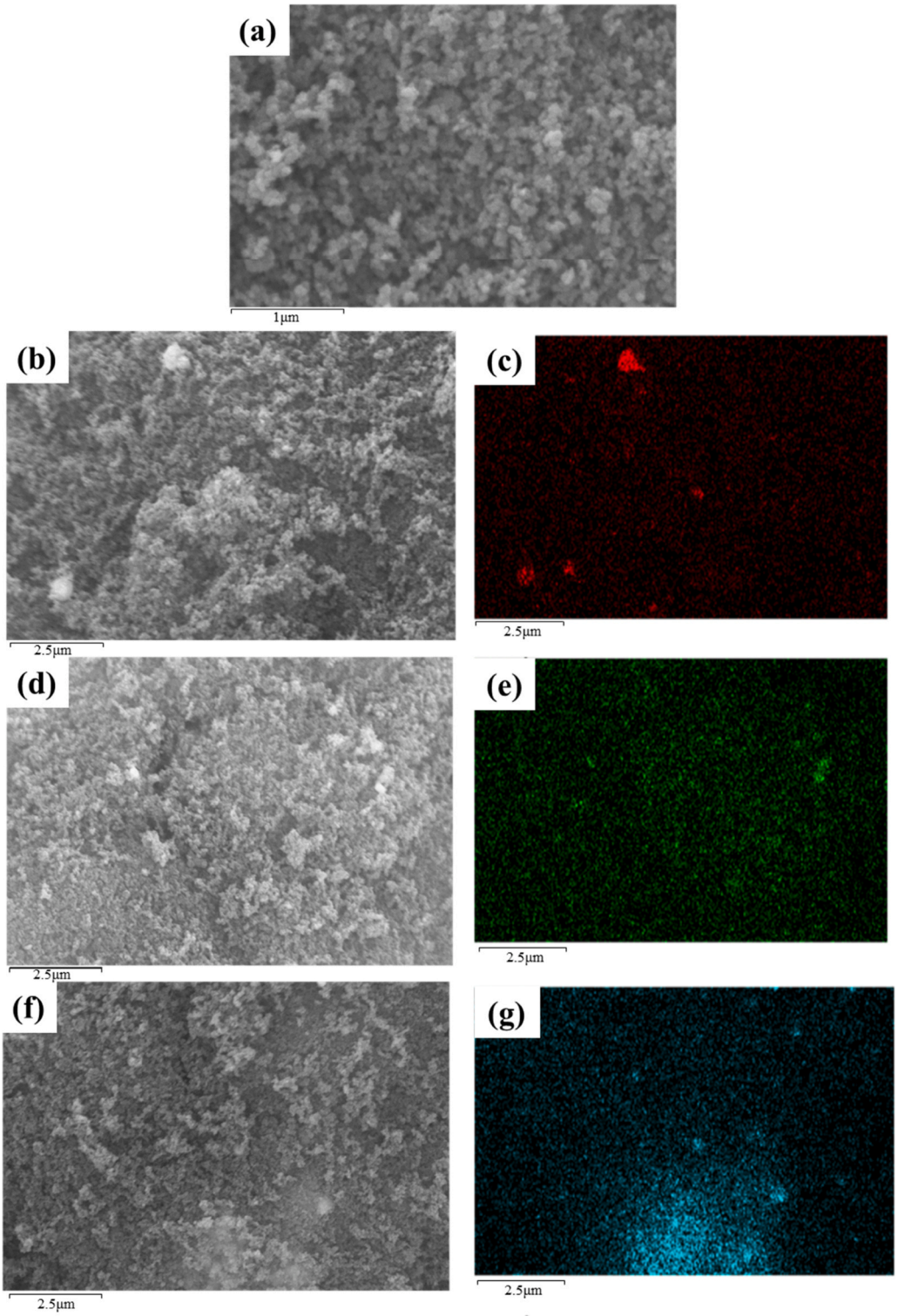

Fig. 6. SEM images and corresponding EDX elemental mapping of the used catalysts. (a) SEM image of the metal-free used carbon; (b) SEM image of used Zn/C; (c) EDX elemental mapping of Zn; (d) SEM image of used Fe/C; (e) EDX elemental mapping of Fe; (f) SEM image of used Cu/C; and (g) EDX elemental mapping of Cu.

particle agglomeration morphology in the SEM, it can be inferred that Zn is mainly in a dispersed state, but its spatial uniformity is lower than that of the fresh sample. This local enrichment may be related to the migration, redeposition, or interaction with surface oxygen-containing groups of Zn species under high-temperature steam and complex volatile atmospheres. The resulting decrease in uniform accessibility of Zn-related sites may contribute to the relatively limited promotion effect of Zn/C on deep reforming reactions. In contrast, the used Fe/C (Fig. 6 (d)-(e)) exhibits a more continuous and homogeneous Fe distribution, without noticeable macroscopic enrichment zones or strip-like aggregation features. This indicates that Fe species maintain good dispersion stability throughout the reaction. Considering the higher gas yield, water consumption, carbon conversion, and hydrogen potential observed for the Fe/C system (Sections 3.2 and 3.3), such dispersion retention can be regarded as an important structural basis for sustaining accessible active sites, facilitating water activation, and promoting the

conversion of reaction intermediates throughout the reforming process. For the used Cu/C catalyst (Fig. 6(f)-(g)), Cu species are still broadly distributed across the carbon surface; however, compared with Fe/C, more obvious signal intensification is observed, suggesting partial enrichment or structural rearrangement of Cu under reaction conditions. Although SEM reveals no significant growth of large Cu particles, the non-uniform elemental distribution suggests that Cu active sites may become less accessible due to migration or aggregation, thereby limiting further enhancement in reforming depth and long-term catalytic stability.

Fig. 7 shows the XRD patterns of the catalysts after the reaction. All used catalysts display broad diffraction features at 2θ≈ 20–25°, characteristic of amorphous or poorly graphitized carbon, indicating that the disordered structure of carbon support is preserved after reaction. This observation is consistent with the morphological stability revealed by SEM analysis. For the Zn/C catalyst, diffraction peaks corresponding to ZnO are observed after the reaction, suggesting that Zn species mainly exist in an oxidized state in the reaction atmosphere. Given the limited redox capability of ZnO, Zn is expected to function mainly as an interface modifier or secondary promoter rather than as a redox-active center, which is consistent with its moderate effect on catalytic performance. For the Fe/C catalyst, characteristic peaks of both Fe_3O_4 and FeO are observed in the XRD pattern, indicating the coexistence of multiple iron oxidation states after reaction. Such mixed-valence Fe species are commonly associated with reversible redox behavior and enhanced water activation capability. The Fe_3O_4/FeO system can promote the dissociation of water molecules and the further oxidation of intermediates through lattice oxygen migration or oxygen vacancy mechanisms, thereby enhancing the steam reforming and water-gas shift reactions. This provides a reasonable structural basis for the higher water consumption, carbon conversion, and hydrogen potential observed over Fe/C in Sections 3.2 and 3.3. For the Cu/C catalyst, the coexistence of metallic Cu^0 and Cu_2O is detected, indicating that Cu species undergo partial oxidation-reduction cycling under reaction conditions. While redox dynamics can contribute to hydrocarbon activation and surface dehydrogenation, they may also be accompanied by structural reconstruction or sintering, in line with the local enrichment observed in SEM-EDX.

Table 3 summarizes the BET surface area and pore volume of the catalysts after the reaction. Compared with the fresh catalysts, only a slight decrease in BET surface area is observed, while the pore volume remains essentially unchanged (0.43–0.44 $cm^3\ g^{-1}$). These results indicate that no significant pore blockage, structural collapse, or excessive irreversible carbon deposition occurs during the reaction. The preservation of pore structure is crucial, as it excludes textural degradation as the dominant factor governing catalytic performance differences. Consequently, the variations in reforming activity and selectivity among the catalysts can be primarily attributed to differences in metal dispersion stability, oxidation state evolution, and metal-intermediate interactions rather than changes in the carbon support structure.

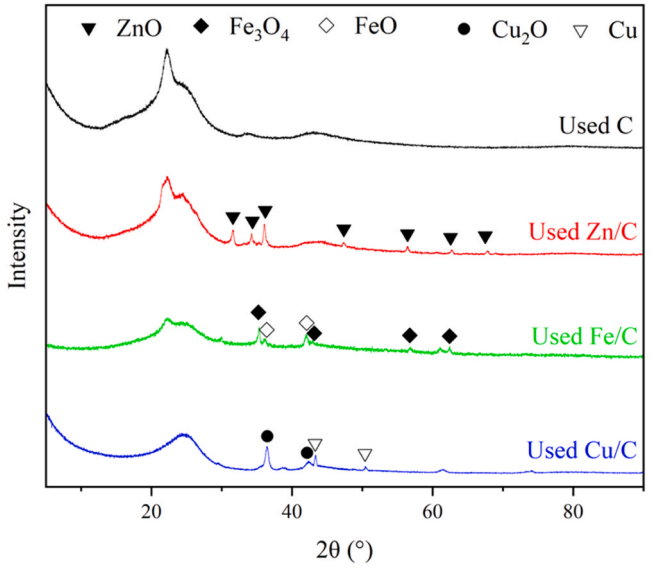

Fig. 7. XRD pattern of the used carbon catalysts.

Table 3
Physical properties of the used catalysts.

	BET surface area (m^2/g)	Pore volume (cm^3/g)
Used Carbon	209.4	0.43
Used Zn/C	221.0	0.43
Used Fe/C	209.3	0.44
Used Cu/C	216.7	0.43

3.5. Discussion of the reaction mechanism

Fig. 8 presents the reaction pathways of the key intermediate (C_2H_4) on the surfaces of different metal-supported carbon catalysts during the pyrolysis-catalytic steam reforming of HDPE, while Fig. 9 provides a quantitative comparison of the energy barriers associated with C_2H_4 dehydrogenation and water activation based on density functional theory calculations. To clearly illustrate the reaction mechanism, only a single layer of metal atoms is depicted in Fig. 8, whereas the calculations were performed with a four-layer model. By combining macroscopic reaction pathway analysis with microscopic kinetics insights, these results reveal the regulatory mechanisms of different metal species on the reaction. As shown in Fig. 8, HDPE undergoes random chain scission during pyrolysis, generating volatiles mainly composed of low-molecular-weight hydrocarbons, among which C_2H_4 is one of the most representative and reactive intermediates. In the absence of metal active sites, ethylene mainly follows gas-phase thermal cracking or non-selective conversion pathways, leading to the formation of CH_4, C_2-C_4 light hydrocarbons and a considerable fraction of CO_2. These reaction pathways limit the efficient conversion of carbon to CO and H_2, consistent with the relatively low syngas yield and hydrogen selectivity observed in the pure carbon system. When the carbon catalyst loaded with metal was introduced, the reaction path changed significantly. Ethylene molecules preferentially adsorb on metal active sites and undergo a stepwise dehydrogenation process, forming intermediates such as C_2H_3* and C_2H_2* in the surface-adsorbed state. Similar reaction pathways have been verified in the DFT study of steam reforming systems for heavy hydrocarbons (such as diesel fuel) [45]. Compared with the surface of pure carbon, metal sites can significantly lower the activation barriers for C-H bond cleavage, transforming ethylene conversion from a gas-phase cracking process into a surface catalytic pathway. Furthermore, as the continuous dehydrogenation of ethylene proceeds, the surface hydrocarbon intermediates can react with the OH* and H* species generated by the dissociation of steam on the metal surface, promoting the formation of CO and H_2. This pathway effectively inhibits the formation of CH_4 and C_2-C_4 hydrocarbons, which are highly consistent with the observed trends in low-light hydrocarbon yield, increased CO selectivity, and increased H_2/CO ratio.

Fig. 9(a) shows the energy profiles and corresponding transition states associated with the stepwise conversion of ethylene on pure carbon as well as on Zn/C, Cu/C, and Fe/C surfaces. In the absence of metal species, the initial activation of ethylene involves relatively high energy barriers, indicating that effective C-H or C-C bond cleavage is kinetically unfavorable on the carbon surface. This theoretical result directly correlates with low carbon conversion and hydrogen potential observed experimentally for the pure carbon catalyst. In contrast, the introduction of metal species significantly reduces the energy barriers of key reaction steps, following the order Fe/C < Cu/C < Zn/C < Carbon. Among them,

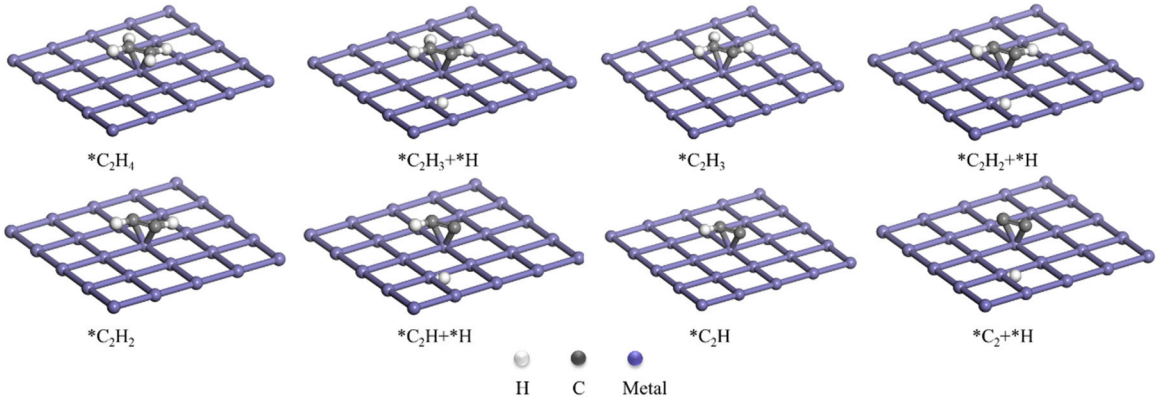

Fig. 8. Proposed reaction pathways of C_2H_4 conversion over metal-supported carbon catalysts during pyrolysis-catalytic steam reforming.

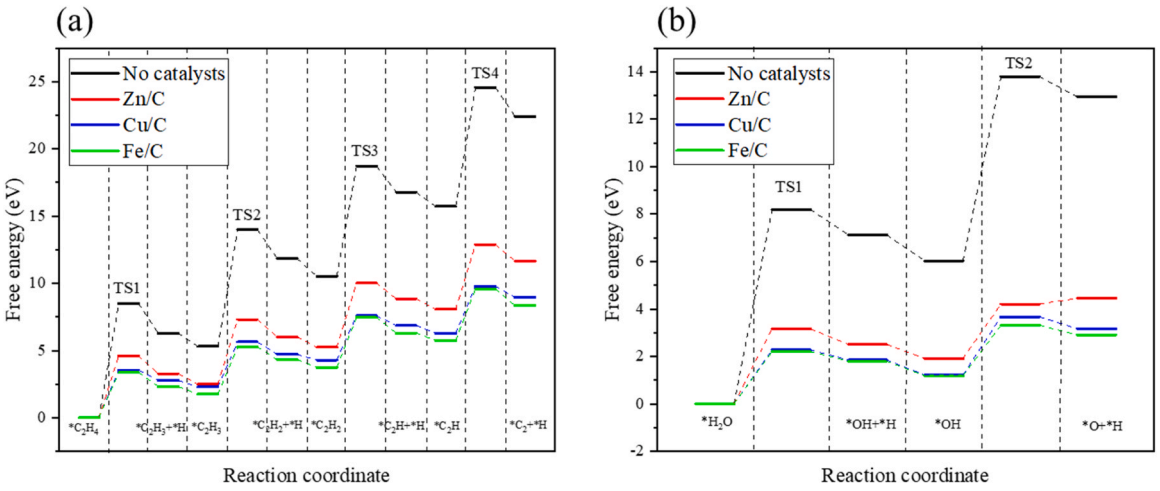

Fig. 9. Reaction energy profiles for C_2H_4 dehydrogenation and water dissociation over different catalysts.

the Fe/C system exhibits the lowest activation barriers for multiple dehydrogenation and cracking steps, indicating the strongest activation ability toward hydrocarbon intermediates. This phenomenon can be attributed to the interaction between the d orbitals of transition metals and the π bond of ethylene, causing partial filling of the antibonding orbitals, thereby weakening the C-H and C-C bond strengths and reducing the energy barrier for their cleavage. The Cu/C system shows a moderate reduction in energy barriers, while the promoting effect of Zn/C remains comparatively limited. This trend is fully consistent with the ranking of gas yield, carbon conversion, and hydrogen potential observed in the experiment.

In the steam reforming system, water molecules are not inert components. Their activation behavior directly determines the availability of surface OH* and H* species. Fig. 9(b) presents the energy barriers associated with the dissociation of water ($H_2O \rightarrow OH^* + H^*$) on different catalyst surfaces. On the pure carbon surface, water dissociation is kinetically hindered by a high energy barrier, indicating limited water activation capability. However, metal-loaded catalysts significantly facilitate water dissociation, with the activation barrier decreasing in the order Fe/C > Cu/C > Zn/C. Notably, Fe/C exhibits the lowest barrier, highlighting its superior ability to activate water molecules. Previous research [46] has shown that surface OH* species play a dual role in the conversion of hydrocarbons. On one hand, OH* can act as a hydrogen donor and reduce the energy barrier for the breaking of C-H bonds through a synergistic mechanism; on the other hand, OH* can participate in the surface oxidation process, promoting the conversion of carbon intermediates to CO and inhibiting the formation of carbon deposits. Therefore, metals not only directly affect the cracking pathways of hydrocarbons, but also indirectly change the entire reaction network by regulating the dissociation ability of water.

Overall, the experimental and theoretical results indicate that metal species regulate the reforming behavior through two coupled mechanisms: (i) direct activation of hydrocarbon intermediates by lowering C-H and C-C bond cleavage barriers, and (ii) indirect promotion of steam-assisted reforming via enhanced water dissociation. These effects are most pronounced for Fe/C, followed by Cu/C and Zn/C.

4. Conclusions

This study systematically elucidates the roles of pure carbon, Zn/C, Cu/C, and Fe/C catalysts in the pyrolysis-catalytic steam reforming of HDPE for syngas production by combining experimental analysis and DFT calculations. Under comparable carbon support structures, the introduction of metal species significantly improves gas yield and syngas yields, and alters carbon conversion pathways, favoring the transformation of carbon from CO_2 and light hydrocarbons into CO and H_2. Among the catalysts studied, Fe/C exhibits the highest gas yield, syngas yield, and hydrogen potential, followed by Cu/C, while the promoting effect of Zn/C is relatively limited.

The structural characterization of the catalysts after the reaction and DFT calculations reveal that metal species regulate the reaction pathways through two coupled mechanisms: lowering the activation barriers for C-H and C-C bond cleavage of hydrocarbon intermediates and promoting water dissociation to generate active OH* and H* species. This synergistic mechanism is most significant in the Fe/C system, which is highly consistent with its excellent experimental performance. Overall,

this work provides guidance for the rational utilization of metal-containing waste-derived char catalysts for hydrogen-rich syngas production in the pyrolysis-catalytic steam reforming process.

Author contributions

Yukun Li conducted the experiments, processed and analyzed the experimental data, and wrote the first draft of the manuscript. **Zhiheng Ma** and **Bingyang Li** performed density functional theory (DFT) calculations and contributed to the theoretical analysis. **Meiqian Chen** and **Hui Zhou** contributed to the conceptual discussion of the results, assisted in organizing the manuscript structure. **Paul T. Williams** designed and supervised the experimental work, and critically revised and edited the final version of the manuscript.

CRediT authorship contribution statement

Paul T. Williams: Writing – review & editing, Supervision, Project administration, Conceptualization. **Hui Zhou:** Supervision, Conceptualization. **Meiqian Chen:** Supervision, Conceptualization. **Bingyang Li:** Investigation, Formal analysis. **Zhiheng Ma:** Investigation, Formal analysis. **Yukun Li:** Writing – original draft, Methodology, Investigation, Formal analysis.

Declaration of Competing Interest

The authors declare that they have no known competing financial interests or personal relationships that could have appeared to influence the work reported in this paper.

Acknowledgements

The authors gratefully acknowledge the financial support provided by the China Scholarship Council-University of Leeds Scholarship, which supported Yukun Li during this research. This work was also supported by the National Natural Science Foundation of China (No. U21B2095) and the UK Royal Society International Exchanges Program in collaboration with the National Natural Science Foundation of China (Grant No. IEC\NSFC\223321) and the Tsinghua-Toyota Joint Research Fund (Grant No. 20253930017). The authors would also like to thank the Bragg Centre for Materials Research at the University of Leeds for help with SEM-EDXS and XRD analysis.

Data availability

Data will be made available on request.

References

[1] R. Geyer, J.R. Jambeck, K.L. Law, Production, use, and fate of all plastics ever made, Sci. Adv. 3 (2017) e1700782.
[2] M.A. Bashir, T. Ji, J. Weidman, Y. Soong, M. Gray, F. Shi, P. Wang, Plastic waste gasification for low-carbon hydrogen production: a comprehensive review, Energy Adv. 4 (2025) 330–363.
[3] V. Mangesh, S. Padmanabhan, P. Tamizhdurai, A. Ramesh, Experimental investigation to identify the type of waste plastic pyrolysis oil suitable for conversion to diesel engine fuel, J. Clean. Prod. 246 (2020) 119066.
[4] T.K. Anh Nguyen, T. Trần-Phú, R. Daiyan, X. Minh Chau Ta, R. Amal, A. Tricoli, From plastic waste to green hydrogen and valuable chemicals using sunlight and water, Angew. Chem. Int. Ed. 63 (2024) e202401746.
[5] A. Midilli, H. Kucuk, M. Haciosmanoglu, U. Akbulut, I. Dincer, A review on converting plastic wastes into clean hydrogen via gasification for better sustainability, Int. J. Energy Res. 46 (2022) 4001–4032.
[6] Y. Shi, X. Diao, S. Zhang, K. Cao, R. Wei, C. Yan, Y. Ma, N. Ji, From waste plastic to hydrogen fuel: selective conversion through advanced catalytic technologies, Appl. Energy 404 (2026) 127144.
[7] Z. Luo, X. Zhu, S. Yu, B. Yu, D. Chen, Z. Ma, X. Zhu, C.C. Xu, H. Zhou, Overcoming limitations in polyolefins upcycling by codesigning endothermic-exothermic magnetocatalytic system, Nano Res. Energy (2025).
[8] S. Czernik, R.J. French, Production of hydrogen from plastics by pyrolysis and catalytic steam reform, Energy & fuels 20 (2006) 754–758.
[9] C. Wu, P.T. Williams, Pyrolysis–gasification of plastics, mixed plastics and real-world plastic waste with and without Ni–Mg–Al catalyst, Fuel 89 (2010) 3022–3032.
[10] P.T. Williams, Hydrogen and carbon nanotubes from pyrolysis-catalysis of waste plastics: a review, Waste Biomass. Valoriz. 12 (2021) 1–28.
[11] I. Barbarias, G. Lopez, M. Artetxe, A. Arregi, J. Bilbao, M. Olazar, Valorisation of different waste plastics by pyrolysis and in-line catalytic steam reforming for hydrogen production, Energy Convers. Manag. 156 (2018) 575–584.
[12] T. Namioka, A. Saito, Y. Inoue, Y. Park, T. Min, S. Roh, K. Yoshikawa, Hydrogen-rich gas production from waste plastics by pyrolysis and low-temperature steam reforming over a ruthenium catalyst, Appl. Energy 88 (2011) 2019–2026.
[13] L. Santamaria, G. Lopez, E. Fernandez, M. Cortazar, A. Arregi, M. Olazar, J. Bilbao, Progress on catalyst development for the steam reforming of biomass and waste plastics pyrolysis volatiles: a review, Energy Fuels 35 (2021) 17051–17084.
[14] D. Yao, H. Yang, H. Chen, P.T. Williams, Co-precipitation, impregnation and so-gel preparation of Ni catalysts for pyrolysis-catalytic steam reforming of waste plastics, Appl. Catal. B Environ. 239 (2018) 565–577.
[15] A. Farooq, H. Song, Y. Park, G.H. Rhee, Effects of different Al_2O_3 support on HDPE gasification for enhanced hydrogen generation using Ni-based catalysts, Int. J. Hydrog. Energy 46 (2021) 18085–18092.
[16] B. Nabgan, M. Tahir, T.A.T. Abdullah, W. Nabgan, Y. Gambo, R. Mat, I. Saeh, Ni/Pd-promoted Al_2O_3–La_2O_3 catalyst for hydrogen production from polyethylene terephthalate waste via steam reforming, Int. J. Hydrog. Energy 42 (2017) 10708–10721.
[17] Y. Zhang, J. Huang, P.T. Williams, Fe–Ni–MCM-41 catalysts for hydrogen-rich syngas production from waste plastics by pyrolysis–catalytic steam reforming, Energy Fuels 31 (2017) 8497–8504.
[18] A. Arregi, M. Seifali, Abbas-Abadi, G. Lopez, L. Santamaria, M. Artetxe, J. Bilbao, M. Olazar, CeO_2 and La_2O_3 promoters in the steam reforming of polyolefinic waste plastic pyrolysis volatiles on Ni-based catalysts, ACS Sustain. Chem. & Eng. 8 (2020) 17307–17321.
[19] D. Yao, H. Yang, H. Chen, P.T. Williams, Investigation of nickel-impregnated zeolite catalysts for hydrogen/syngas production from the catalytic reforming of waste polyethylene, Appl. Catal. B Environ. 227 (2018) 477–487.
[20] Y. Li, M.A. Nahil, P.T. Williams, Pyrolysis-catalytic steam reforming of waste plastics for enhanced hydrogen/syngas yield using sacrificial tire pyrolysis char catalyst, Chem. Eng. J. 467 (2023) 143427.
[21] Y. Li, P.T. Williams, Catalytic steam reforming of waste tire pyrolysis volatiles using a tire char catalyst for high yield hydrogen-rich syngas, Fuel Process. Technol. 265 (2024) 108150.
[22] Y. Li, M.A. Nahil, P.T. Williams, Hydrogen/syngas production from different types of waste plastics using a sacrificial tire char catalyst via pyrolysis–catalytic steam reforming, Energy Fuels 37 (2023) 6661–6673.
[23] Z. Yao, G. Xia, W. Cao, K. Zeng, Y. Wang, Mechanistic exploration of furfural hydrogenation on copper surface in aqueous phase by DFT and AIMD simulations, J. Catal. 418 (2023) 1–12.
[24] X. Zou, M. Zhai, D. Yang, G. Liu, T. Wang, L. Guo, Y. Zhang, New insights into the mechanism of biomass char steam gasification process by oxygen-containing functional group as aromatic carbon boundaries: experimental and DFT study, Chem. Eng. J. 465 (2023) 142947.
[25] H. Chen, J. Meng, X. Wang, S. Ma, C. Bu, J. Zhang, C. Liu, H. Xie, Insights into the adsorption and decomposition mechanisms of tar typical model compounds (benzene, toluene and phenol) on Ni (111) surface by DFT calculations, J. Energy Inst. 114 (2024) 101602.
[26] Z. Wei, Y. Li, Y. Zhang, W. Liu, K. Han, R. Sun, A DFT study on catalytic cracking mechanism of tar by Ni or Fe doped CaO during biomass steam gasification, Fuel 374 (2024) 132468.
[27] P. Zhou, X. Li, J. Zhou, Z. Peng, L. Shen, W. Li, Insights of the adsorption mechanism of methylene blue on biochar from phytoextraction residues of Citrus aurantium L.: adsorption model and DFT calculations, J. Environ. Chem. Eng. 11 (2023) 110496.
[28] S. Zhang, Y. Gao, S. Xu, X. Bie, J. Niu, Q. Li, Y. Zhang, H. Zhou, Size-dependent structural transitions dictate synergy and function in Ni-Ru bimetallic catalysts, Angew. Chem. (2026) e4017792.
[29] G. Kresse, J. Furthmüller, Efficiency of ab-initio total energy calculations for metals and semiconductors using a plane-wave basis set, Comput. Mater. Sci. 6 (1996) 15–50.
[30] J.P. Perdew, K. Burke, M. Ernzerhof, Generalized gradient approximation made simple, Phys. Rev. Lett. 77 (1996) 3865.
[31] S. Grimme, J. Antony, S. Ehrlich, H. Krieg, A consistent and accurate ab initio parametrization of density functional dispersion correction (DFT-D) for the 94 elements H-Pu, J. Chem. Phys. 132 (2010).
[32] J. Paier, R. Hirschl, M. Marsman, G. Kresse, The Perdew–Burke–Ernzerhof exchange-correlation functional applied to the G2-1 test set using a plane-wave basis set, J. Chem. Phys. 122 (2005).
[33] R. GuilLopez, J. Botas, J. Fierro, D. Serrano, Comparison of metal and carbon catalysts for hydrogen production by methane decomposition, Appl. Catal. A Gen. 396 (2011) 40–51.
[34] P. Thirukumaran, R. Balasubramanian, R. Atchudan, A.S. Parveen, Y.R. Lee, S.-C. Kim, Metal-free nitrogen-rich glassy carbon as an electrocatalyst for hydrogen evolution reaction, Mater. Res. Bull. 124 (2020) 110734.
[35] C. Sasirekha, S. Arumugam, G. Muralidharan, Green synthesis of ZnO/carbon (ZnO/C) as an electrode material for symmetric supercapacitor devices, Appl. Surf. Sci. 449 (2018) 521–527.

[36] H. Xu, S. Lv, W. Wu, W. Gao, M.H. Tahir, X. Guo, S. Zhang, Catalytic conversion of the heavy fraction of bio-oil into phenol-rich oils using an Fe-carbon catalyst during straw pyrolysis, J. Anal. Appl. Pyrolysis 186 (2025) 106902.
[37] B. Tian, S. Mao, F. Guo, J. Bai, R. Shu, L. Qian, Q. Liu, Monolithic biochar-supported cobalt-based catalysts with high-activity and superior-stability for biomass tar reforming, Energy 242 (2022) 122970.
[38] S. Zhang, X. Bie, Z. Qian, M. Wu, K. Li, Q. Li, Y. Zhang, H. Zhou, Synergistic interactions between cellulose and plastics (PET, HDPE, and PS) during CO2 gasification-catalytic reforming on Ni/CeO2 nanorod catalyst, Appl. Energy 361 (2024) 122975.
[39] G. Yang, Q. Hu, J. Hu, H. Yang, S. Yan, Y. Chen, X. Wang, H. Chen, Hydrogen-rich syngas production from biomass gasification using biochar-based nanocatalysts, Bioresour. Technol. 379 (2023) 129005.
[40] T. Qin, S. Yuan, Research progress of catalysts for catalytic steam reforming of high temperature tar: A review, Fuel 331 (2023) 125790.
[41] T. An, Z. Zhang, X. Ren, K. Wang, Z. Li, M. Li, Fe doping promotes water splitting activity of nickel-based catalysts in steam reforming of tar model compound, Appl. Catal. A Gen. (2025) 120424.
[42] Y. Wu, C. Pei, H. Tian, T. Liu, X. Zhang, S. Chen, Q. Xiao, X. Wang, J. Gong, Role of Fe species of Ni-based catalysts for efficient low-temperature ethanol steam reforming, Jacs Au 1 (2021) 1459–1470.
[43] A.A. Mirzaei, M. Arsalanfar, H.R. Bozorgzadeh, A. Samimi, A review of Fischer-Tropsch synthesis on the cobalt based catalysts, Phys. Chem. Res. 2 (2014) 179–201.
[44] Y. Wang, P. Hu, J. Yang, Y.-A. Zhu, D. Chen, C–H bond activation in light alkanes: a theoretical perspective, Chem. Soc. Rev. 50 (2021) 4299–4358.
[45] Q. Xue, Z. Li, Z. Jiang, M. Chen, B. Yan, Y. Wang, G. Luo, Effect of characteristic component on diesel steam reforming to hydrogen over highly dispersed Ni–Rh- and Ni-based catalysts: Experiment and DFT calculation study, Fuel 303 (2021) 121306.
[46] D. Hibbitts, M. Neurock, Promotional effects of chemisorbed oxygen and hydroxide in the activation of C-H and O-H bonds over transition metal surfaces, Surf. Sci. 650 (2016) 210–220.